AIAA Journal
Vol. 47, No. 2, February 2009

Evolutionary Optimization of a Morphing Wing with Wind-Tunnel Hardware in the Loop

Frank Boria,* Bret Stanford,* Scott Bowman,* and Peter Ifju†
University of Florida, Gainesville, Florida 32611

DOI: 10.2514/1.38941

Active wing morphing is a fertile technology in the realm of unmanned and micro air vehicles: low flight loads and flexible wing materials allow substantial deformation with relatively low actuation power. Proper shape management of these wings for maximum performance is challenging: numerical optimization methods may struggle to accurately predict the three-dimensional flow separation, transition, and reattachment expected at the low operating Reynolds numbers. Conventional experimental optimization techniques (a response surface fit through a designed experiment) may be unable to represent the discontinuous functions commonly seen in aerodynamic applications, and the number of function evaluations can become overwhelming with multilevel actuation mechanisms. This paper outlines an effective experimental technique for shape management optimization of a morphing airfoil: a genetic algorithm with wind-tunnel hardware (strain-gauge sting balance) in the loop. Optimal wing shapes are found to maximize the measured lift or efficiency through the sweep of angles of attack, by allowing the wing's shape control to be defined through deformation at a single actuation point (camber control) or two actuation points (camber and reflex control). Aerodynamic and electrical hysteresis limits the repeatability of sting-balance measurements, complicating the convergence of the genetic algorithm, but not preventing the adequate location of optimal designs.

Nomenclature

α = angle of attack
C_D = coefficient of drag
C_L = coefficient of lift
$C_{L\alpha}$ = lift slope
c = chord
L/D = efficiency
N = number of morphing servos
sp = servo position
U_∞ = freestream velocity
x, y, z = Cartesian coordinates

I. Introduction

RAPID advancements in actuator and material technologies have enabled the use of practical wing morphing platforms: aircraft are no longer confined to fixed wing geometries that can only suit a single flight regime. Such a capability allows for optimal wing shapes for a disparate array of flight maneuvers. Active wing morphing is a biologically inspired concept: birds constantly change their wing shape to successfully undertake glides, descents, and aggressive maneuvers [1]. Along this analogy, a versatile morphing aircraft can achieve high lift for maximum payload-carrying capacity, high speed to quickly move from waypoint to waypoint, or high efficiency during cruise flight [2]. Using a morphing structure with asymmetric deformations can provide highly agile maneuvering through complex urban environments. Such a vehicle can also maintain stability through the most volatile of flight conditions, such as erratic and gusty airflow among buildings and structures. Active morphing is a particularly attractive option for unmanned and micro air vehicles (MAVs): low flight loads and highly flexible wing structures allow a relatively small amount of actuation energy to inflict a substantial shape change over the wing. Furthermore, active morphing strategies can provide the designer with an additional tool to alleviate poor efficiency characteristics (as necessitated by the low Reynolds numbers inhabited by such vehicles: 10^4–10^5) and weight management challenges (typically for static stability via the c.g. location) known to hinder the practicality of such vehicles.

With the ever-increasing complexity of morphing mechanisms comes the challenge of proper shape management to achieve desirable real-time flight characteristics. The work presented in this paper is one approach to such a challenge. A closed-loop wind tunnel with a strain-gauge sting balance is used as a hardware-in-the-loop objective function for optimizing a multiple-design-variable morphing wing structure. The optimal airfoil shape (found by varying the camber and/or reflex) is located to maximize lift or efficiency for a range of prestall angles of attack, using a conventional evolutionary genetic algorithm (GA). Such a strategy must be thought of as a more efficient means of experimental optimization (when compared with conventional response-surface-based techniques) as the number of design variables increases. Although only two are considered in this work (actuation at two locations along the wing root), the general technique is successfully demonstrated, permitting future research in a larger design space. Furthermore, the complex and poorly understood flowfields about low-aspect-ratio MAV wings at low Reynolds numbers also limits the usefulness of conventional numerical optimization schemes.

Several examples of efficient wing morphing mechanisms can be found in the literature. Abdulrahim et al. [3] demonstrate the use of a set of torque rods imbedded in a membrane micro air vehicle wing: actuation of the rods asymmetrically twists the wing for roll control. Similar mechanisms were used to control the Wright Flyer, with active wing twisting facilitated by a series of cables. More complex morphing methods (other than simple rods and cables, for example) can also be considered for wing design. The electroactive polymer actuator [4] is similar to muscle tissue, with regard to stress and force output, and is capable of large-scale linear motion. Macrofiber composites are a thin compliant actuator constructed of orthogonal layers of unidirectional piezoceramic fibers and copper electrodes encased in layers of acrylic and Kapton [5]. Strelec et al. [6] discuss the use of shape memory alloys for wing morphing, noting a specific need to prevent variations in temperature for successful implementation.

Early numerical airfoil optimization work is found in the work of Hicks et al. [7], who use a gradient-based feasible direction method to

---

Received 4 June 2008; revision received 16 September 2008; accepted for publication 9 November 2008.

*Research Assistant, Department of Mechanical and Aerospace Engineering.

†Professor, Department of Mechanical and Aerospace Engineering.

optimize low-drag transonic airfoils. Further gradient-based applications are presented by Lian et al. [8], who conduct shape optimization of a low-aspect-ratio micro air vehicle wing. A sequential quadratic programming optimizer is used in conjunction with a Navier–Stokes solver to maximize the lift-to-drag ratio by varying a series of control points over the wing, with constraints on the wing shape's convexity. Obayashi and Tsukahara [9] discuss the use of three distinct schemes for airfoil optimization: gradient-based, simulated annealing, and evolutionary genetic algorithms. The genetic algorithm is found to be superior, despite requiring a larger number of function evaluations. This is thought to be due to a smaller dependence on the initial design, as well as the presence of potentially discontinuous aerodynamic objective functions. A genetic algorithm is implemented by Namgoong et al. [10] for airfoil optimization with strain energy (for the actuators to morph from one shape to the next) as an objective function, along with lift and drag. XFOIL [11] is used to construct a Pareto tradeoff curve between aerodynamic and actuator costs. Higher-fidelity genetic-algorithm optimizations are given by Naujoks et al. [12], who use a turbulent Navier–Stokes solver. Further applications of numerical airfoil optimization fall under the guise of inverse design methods: varying the airfoil shape to minimize the difference between computed pressure distributions and known favorable distributions [13]. Gopalarathnam and Selig [14] conduct such an inverse design for low-speed airfoils, providing insight into the relationship between thickness and efficiency at low Reynolds numbers.

Experimental optimization with hardware-in-the-loop is a relatively rare undertaking: nonaeronautical examples include the work of Peng et al. [15], who analyze a flat rectangular membrane via three tension forces applied to each edge. The deformed profile of the membrane is optically measured and fed into a genetic algorithm to find the combination of forces that will minimize the wrinkling amplitude. Hemker et al. [16] optimize walking speed and stability with a humanoid robot hardware in the loop, using sequential surrogate quadratic programming with stochastic approximations to the objective functions. Aeronautical applications are given by Hunt et al. [17], who use a genetic algorithm to optimize the forward velocity and motor efficiency of a tethered ornithopter, with flapping rate and tail position as design variables. The authors report several unexpected optimal configurations. Finally, the work of Levinsky and Palko [18] is of most interest to the current research paradigm: shape optimization of a three-dimensional flexible model of an F-111 transonic aircraft technology (TACT) aircraft wing in the wind tunnel at both low and transonic speeds. Twelve actuator locations are used over the wing for both spanwise and chordwise morphing, for constrained minimization of drag using a gradient-projection method. Reported difficulties include wing-shape repeatability, wing degradation, drag measurement repeatability and quality, and enforcement of actuator displacement constraints.

The remainder of this work is outlined as follows. A complete description of the experimental hardware and setup will be given, followed by an account of the numerical evolutionary genetic algorithm, and a visual image correlation system used to measure the wing shapes. Two methods are then described to conduct the wing's shape management optimization. A morphing wing with a single actuator is built to estimate the potentially detrimental effects of experimental hysteresis and to validate the optimal designs (through a comparison with conventional response-surface optimization). Finally, a morphing wing with two actuator inputs is used to determine shapes with optimal lift and efficiency for an array of flight conditions. These two cases represent one- and two-design-variable optimization design studies, in which the variable is the deformation of the wing at the actuation location (the location being fixed). As such, the work described subsequently can be classified as wing-shape management optimization, with the morphing wing design held fixed.

II. Hardware-in-the-Loop Apparatus and Procedure

There are four primary subsystems used in the experimental setup. These include the optimization software, the servo controller, the wind tunnel, and the data acquisition software. Through the use of simple text-format software, data are passed between each of these subsystems. This cooperative scheme of using previously independent software programs provides the means for automating the optimization procedure. A visual image correlation (VIC) system is used independently during testing to determine the three-dimensional wing shapes of noteworthy servo positions.

A. Wind Tunnel

The test facility used for the entirety of this work is a closed-loop wind tunnel (model 407B, Engineering Laboratory Design, Inc.), with the flow loop arranged in a horizontal configuration. The test section has an inner dimension of 0.84 m on each side and is 2.44 m long. The velocity range is between 2 and 45 m/s (maximum Reynolds number of 2.7×10^6), provided by a 250 hp motor and a 2-stage axial fan. Centerline turbulence levels have been measured on the order of 0.2%. Optical access is available on the sidewalls and the ceiling. A Heise model PM differential pressure transducer is attached to a pitot-static tube located at the center of the section's entrance, and a four-wire resistance temperature detector mounted to the wall of the test section measures the airflow temperature.

B. Strain-Gauge Sting Balance

An Aerolab 01-15 6-component strain-gauge sting balance is used to measure the aerodynamic forces and moments of the wind-tunnel models. Each of the six channels is in a full Wheatstone-bridge configuration, with 5 channels dedicated to force and 1 to a moment. Data acquisition is done with a National Instruments (NI) SCXI 1520 8-channel programmable strain-gauge module with full-bridge configuration, 2.5 excitation volts, and a gain of 1000. A NI 6052 DAQPad fire wire provides A/D conversion, multiplexing, and the PC connection. For a given flight condition, the output signals from the 6 components are sampled at 1000 Hz for 2 s. The average of these data is sent to a LabVIEW-based module for the calculation of the relevant aerodynamic coefficients. The sting balance is mounted to a custom-fabricated aluminum model arm within the test section. The arm extends through a hole in the section wall and is then attached to a gearbox and a brushless servomotor system for angle-of-attack control (rates on the order of 1 deg/s). Tunnel speed, model inclination, and force/moment measurements are set/acquired using a dedicated PC and in-house LabVIEW-based software. A schematic of the wind-tunnel setup can be seen in Fig. 1.

C. Servo Controller

Morphing actuation is provided by a set of Futaba S3102 servo actuators. These servos supply $4.6\ \mathrm{kg \cdot cm}$ of torque at a rate of 300 deg/s, with a complete range of 120 deg. Using MATLAB, the position of each servo is commanded through a serial port in a 1200 baud rate, 8 bit, 1 stop, no-parity form. A submodule converts the

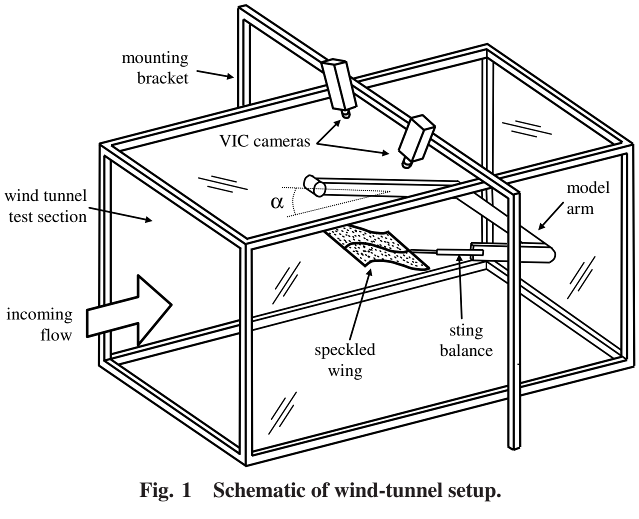

Fig. 1 Schematic of wind-tunnel setup.

RS232 signal to transistor-to-transistor logic. A custom servo controller onboard the morphing wing wind-tunnel model receives the signal. The controller features 8 kB of flash memory, a 16 bit high-resolution servo timer, and an 8 MHz ATMEL microprocessor. This servo controller is able to set and hold 250 different commanded servo positions while the wing undergoes aerodynamic loading.

D. Genetic Algorithm

Airfoil optimization is provided by a genetic algorithm: a stochastic evolutionary algorithm that mimics certain aspects of natural selection observed in biology [19]. Distinct morphing wing shapes are grouped together in a population; the initial populations can be either randomly or uniformly distributed over the design space. The performance (fitness) of each design is then evaluated (using the wind-tunnel/sting-balance hardware). A stochastic process is then used to select the designs that will be used to breed the next generation: designs with higher fitness are more likely to be selected. A certain portion of the fittest designs are directly copied to the next generation (elitism), whereas the rest of the selected designs are paired off for crossover. A child design is created from two parents and typically contains many of the traits of both (reproduction). Mutation is occasionally employed to promote diversity within the population by randomly switching a portion of a design from one generation to the next. Although the relatively expensive genetic algorithm requires a large number of function evaluations (as compared with gradient-based methods), it is employed here for the aforementioned reasons: less dependence on the initial design and a smaller propensity to converge on a local optimum [9]. A third reason comes from purely experimental considerations: sensitivities would have to be computed from a finite difference equation, an entity that can be greatly distorted by even minor amounts of error or noise.

MATLAB's Genetic Algorithm Toolbox [20] is employed for the current work. Morphing wing designs are described by N integers (each integer ranges from 1 to 250, corresponding to the extremes of the servo positions), where N is the number of servos used to morph the wing. Several different population sizes are used, from 10 to 25. The elitism count is set to 2, reproduction is via a 2-point crossover function with a 0.8 crossover fraction, and a uniform mutation function is used with a 0.01 mutation rate. No specific convergence criterion is used; when several generations pass with little change in the population's designs, the process is manually terminated. Less than 30 generations are typically adequate.

E. Optimization Procedure

The two primary software packages used for this study are LabVIEW (for wind-tunnel control and data acquisition) and MATLAB (for wing morphing control and optimization). A flowchart of how the information is passed between the programs is shown in Fig. 2. To initiate the optimization procedure, an initial population is prescribed to the genetic algorithm. The first member of the initial population is then sent to a subroutine that commands the servo controller to morph the wing. These servo positions are simultaneously sent to a text file. The genetic algorithm then waits for the data associated with the servo positions (design fitness) to be added to the text file: this is done by monitoring the text-file size (checking every 0.2 s). Although the optimization software is on hold for data, the wind tunnel is brought up to the required velocity. After the angle of attack is set, the force and moment data are determined from the sting balance. The text file previously created by the optimization software is accessed and these data are appended to the same line. At this point, the data acquisition software waits for the next set of servo positions to be added to the text file. As with the optimization software, the file size is constantly monitored. When the new servo positions are added to the text file, the file size will increase, thereby triggering the data acquisition software for the next set of data. After the force and moment data have been added to the text file, the optimization software identifies the increase in file size and then accesses the data. The next servo positions are commanded, thereby beginning the cycle again.

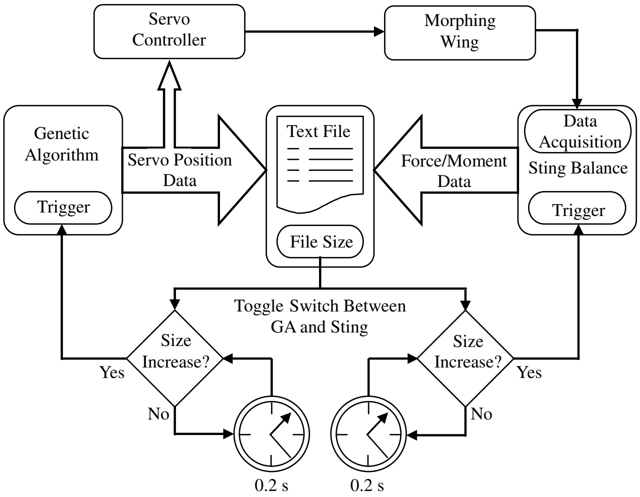

Fig. 2 Flowchart for hardware-in-the-loop optimization.

As with any sting balance, signal drift of the strain gauges is a concern, due to both environment and self-heating. To manage this signal drift, the wind-tunnel software is set to count the number of data sets collected. After a prescribed number, the tunnel velocity is set to zero and the model arm is rotated to the original angle of attack (typically zero). At this point, the data acquisition software performs an offset nullification of the strain-gauge voltages. Then the tunnel is brought back up to the velocity and angle of attack required by the experiment. This simple procedure helps to ensure data quality; the prescribed number of data sets is conveniently set to coincide with the size of the genetic algorithm's population.

F. Visual Image Correlation

VIC is a noncontacting full-field measurement technique [21] used to measure the shape of the morphing wind-tunnel models under aerodynamic loading. The system is only used to quantitatively assess the optimal (or otherwise noteworthy) wing shapes and is not included in the optimization process. The underlying principle of the VIC system is to calculate the shape of a test specimen by digitally acquiring a random speckling pattern applied to the surface. This is done with twin synchronized precalibrated cameras installed over the wind tunnel, as seen in Fig. 1. The VIC system can also measure the displacement field of a structure (useful in measuring aeroelastic deformation of the flexible wings) by tracking a subset of the speckling pattern from one image to the next: temporal matching. For the imaging parameters, wing shapes, and speckling patterns used in the current work, the displacement/shape resolution is estimated to be 0.05 mm.

III. One-Design-Variable Morphing Wing

A. Model Description

To validate the data collection procedures, a morphing wing with a single design variable is used. The rectangular planform wing is fabricated from a single layer of plain-weave carbon-fiber-reinforced plastic (with fibers aligned in the ±45 deg directions), with horizontally aligned unidirectional carbon fiber strips that run from wingtip to wingtip, spaced every 2.5 cm from the leading edge (as seen in Fig. 3). These strips transfer loads such that morphing the wing shape at the root effectively extrudes the same shape up to the wingtip. The root chord of the rectangular wing is 19.5 cm, the wing span is 25.5 cm, the aspect ratio is 1.3, and the wing area is 497 cm^2. At $U_\infty = 16\ \mathrm{m/s}$, the Reynolds number at the root is 200,000. The random speckling pattern applied to the suction surface of the wing can also be seen in Fig. 3 to facilitate measuring the wing shape/deformation with the VIC system.

Actuation is provided with a single morphing servo; the corresponding control horn is attached to the root at $x/c = 0.28$ and is largely constrained to vertical cambering motion. The wing shape

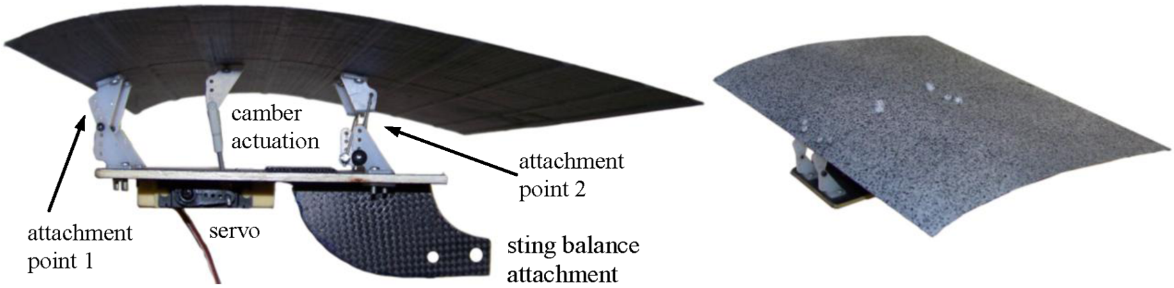

Fig. 3 One-design-variable morphing rectangular wing.

is constrained through two attachment points: one at the leading edge (which permits just rotation) and a second at $x/c = 0.65$ (which permits rotation and some chordwise motion). The servo and the constraint linkages are attached to a mounting platform located below the wing at $z/c = -0.2$. A sting-balance attachment point is also built into the mounting bracket. The full range of actuation will include significant changes in the wing's angle of incidence due to the unconstrained trailing edge (which will also result in an aeroelastic nose-down geometric twist for adaptive washout). To facilitate a comparison of aerodynamic performance of different wing shapes at the same flight condition, the angle of attack is measured with respect to the rigid mounting platform.

The capabilities of the full-field VIC system are demonstrated in Fig. 4, in which the chord-normalized wing-shape contour is plotted, along with airfoil sections at the wing root and the wingtip. It can be seen that the spanwise stiffeners (carbon fiber strips) built into the wing effectively transfer the shape from the actuation points to the wingtip. No change in the camber is noted, though minor aerodynamic twist can be seen at the leading and trailing edges of the wing root (less than 1% of the chord). Using the VIC system, 9 servo positions are selected and photographed to determine the range of attainable wind-off wing shapes. The morphing mechanism is capable of altering the camber from −7 to 19%; normalized root airfoils are plotted in Fig. 5. The location of this camber is variable as well: decreasing the servo position from 250 to 90 shifts the camber location from $x/c = 0.32$ to 0.45. A further decrease in servo position returns the camber location back to 0.32. Passive aeroelastic effects are documented in Fig. 6 for the two extremes of the wing motion (servo positions 1 and 250) at a moderate angle of attack. Minimal passive deformation is observed for the negatively cambered wing, though a slight decambering is observed for the other extreme: the servo is unable to completely hold the wing shape under load, as the camber decreases from 19.1 to 18.4%. The aforementioned washout can also be seen, decreasing the incidence at the root by 4.3 deg.

B. Hysteresis Assessment

Several potential pitfalls exist in the wind-tunnel testing of the wing shown in Fig. 3. The first concern is the electrical hysteresis/resolution/drift of the strain-gauge sting balance [22]. The forces generated by a micro air vehicle may not be more than a few percent of the maximum measurable load of each channel. The lowest measured drag force is 0.2 N (invariably measured from the wing when morphed to a flat plate at a 0 deg angle of attack); such a force will correspond to microvolts across the strain gauges, which introduces a challenging data processing and signal conditioning problem. A second concern is the repeatability of the shapes obtained from the morphing servos, a complaint reported in the work of Levinsky and Palko [18]. The final and most important concern is a viscous effect: Mueller [23] shows that the location of the laminar flow separation, transition, and turbulent reattachment over a

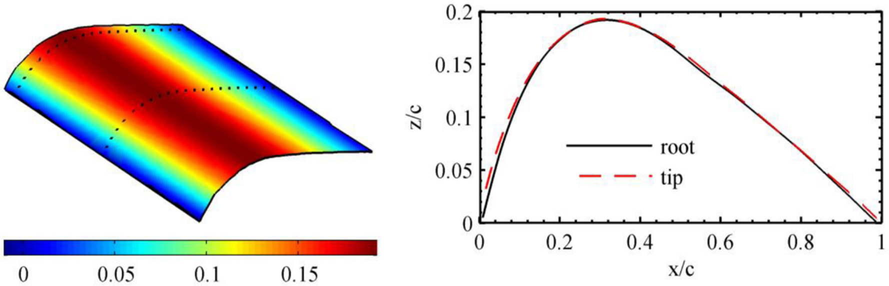

Fig. 4 Measured wind-off wing surface z/c at servo position 250, with sections plotted at the root and the tip.

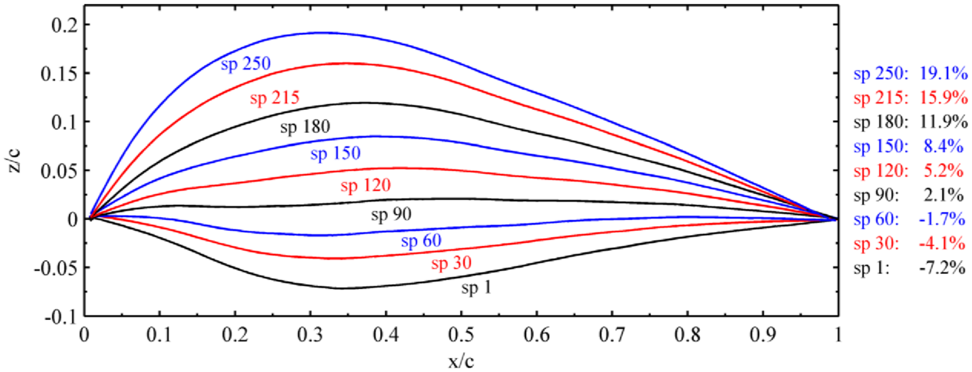

Fig. 5 Measured wind-off root airfoils of the one-design-variable morphing wing model (sp denotes servo position).

Lissaman 7769 and a Milet M06-13-128 airfoil is prone to aerodynamic hysteresis between Reynolds numbers of 60,000 and 300,000 (a range that includes the current application). Differing lift and drag curves are measured, depending on whether the angle of attack is decreasing or increasing, and may also be a problem with a low Reynolds number airfoil that semirandomly changes its shape.

In an effort to determine the effect, if any, of the preceding factors, the following test is conducted. Five servo positions are used to represent the extreme and intermediate positions within the range of motion. Although holding the angle of attack and airspeed constant, 10 consecutive data sets are collected for each of the five servo positions. For each position, this is done without nulling the sensors or changing the shape between measurements; the results should reflect the sting-balance drift and resolution, not aerodynamic hysteresis. Data are then collected as the servo position is randomly altered among the five preselected positions. These data can then be sorted into common servo positions for comparison with the previous test; measured coefficients of variation are given for C_L (Table 1) and C_D (Table 2) in the low-drag, high-lift, and near-stall flight regimes.

The experimental scatter in both signals is acceptable: less than 2.3% coefficient of variance (COV) in lift and less than 3.4% in drag. Measurement errors and repeatability are expected to be worse for the drag, as the relatively small forces reside closer to the sting balance's resolution. Drag forces will also be more susceptible to the viscous flow hysteresis discussed previously. Furthermore, only the lift force shows a distinct trend between the two measurement methods (an order-of-magnitude increase in scatter when the servo position is randomly altered); no such pattern emerges from the drag data. The largest coefficients of variation are typically measured from the negatively cambered airfoil at servo position 1 (as seen in Fig. 5). Significant leading-edge flow separation can be expected even at low and moderate angles of attack. In addition to the turbulent reattachment issues, unsteady leading-edge vortex shedding may distort what is essentially a static sting-balance measurement.

C. Alpha-Sweep Results

The lift coefficient (Fig. 7), drag coefficient (Fig. 8), and lift-to-drag ratio (Fig. 9) are given as a function of angle of attack for the same nine servo positions that populate Fig. 5. As expected, altering the camber has no significant effect on the prestall lift slope: the average $C_{L\alpha}$ is 0.047, which is characteristically shallow for the low-aspect-ratio wing. An increase in the slope is seen for the aggressively cambered airfoils (up to 0.064), possibly due to the nonlinear vortex lift generated by the tip-vortex swirling system. Otherwise, the lift curve is largely shifted up or down, with the zero-lift angle of attack ranging from 5.1 to −10.6 deg (extrapolated). The stalling angle and the maximum C_L progressively increase with actuation up to 12% camber, after which stall is very benign and poorly defined. This latter effect may be due in part to the adaptive washout shown in Fig. 6, a mechanism known to cause such behavior [8]. Distinct trends are harder to discern for the drag data of Fig. 8. Airfoil cambers between −5 and 5% exhibit similar drag performance at small and moderate angles of attack (though a clear trend develops closer to stall, as exaggerated camber increases drag). The wing morphed to servo position 60 (−2% camber) appears to show the drag bucket commonly associated with transitional flows over low Reynolds number airfoils [23].

Table 1 Measured scatter in the coefficient of lift at $U_\infty = 16$ m/s

Servo position	Measurement method	COV, %		
		$\alpha = 0$ deg	$\alpha = 10$ deg	$\alpha = 22.5$ deg
SP1	Consecutive	0.14	0.32	1.79
	Random	1.36	2.20	2.28
SP 125	Consecutive	0.34	0.21	0.25
	Random	1.17	0.98	1.45
SP 250	Consecutive	0.19	0.38	0.30
	Random	0.83	0.25	1.36

Table 2 Measured scatter in the coefficient of drag, $U_\infty = 16$ m/s

Servo position	Measurement method	COV, %		
		$\alpha = 0$ deg	$\alpha = 10$ deg	$\alpha = 22.5$ deg
SP1	Consecutive	3.07	3.40	1.90
	Random	2.63	2.29	1.67
SP 125	Consecutive	0.56	1.85	0.81
	Random	0.87	1.22	1.26
SP 250	Consecutive	1.29	1.05	0.39
	Random	1.47	0.69	1.24

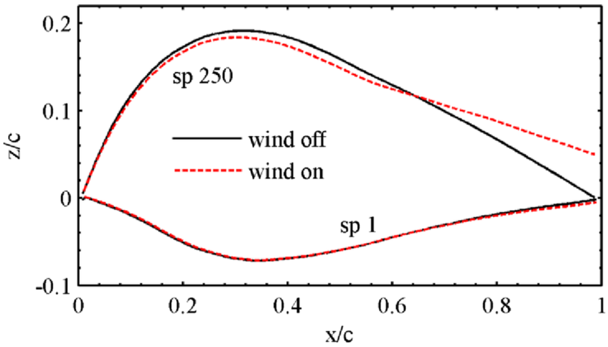

Fig. 6 Passive aeroelastic wing deformation at $U_\infty = 16$ m/s and $\alpha = 10$ deg.

The trends in the lift-to-drag ratio (Fig. 9) as a function of camber are similarly difficult to predict. Highly cambered airfoils are preferred at negative and poststall angles of attack, whereas moderate camber (5%) is optimal for most of the range in between. The exception is at 7.5 and 10 deg angles of attack, where the slightly negatively cambered airfoil at servo position 60 is measured with the highest efficiency; this performance is certainly drag-based (rather than lift-based), predominately due to the aforementioned bucket. The rapid changes in drag between servo positions 30, 60, and 90 indicate the superiority of a evolutionary genetic algorithm over a gradient-based search optimization, which would struggle with the discontinuous objective functions present at low Reynolds numbers. The systematic data presented in these three figures can now be used to validate the hardware-in-the-loop optimization procedure, as the optimal wing shape (in terms of lift, drag, or efficiency) is known for a sweep of angles of attack (to within 30 servo positions).

D. Validation of Optimization Procedure

The evolutionary optimization of the wing's lift at a 10 deg angle of attack is given in Fig. 10. In addition to the GA specifications given previously, a population size of 11 is used, initially uniformly distributed within the design space (between servo positions 1 and 250). The results from the function evaluations of each design in each generation are plotted through 13 generations (at which point suitable convergence is achieved). These data are overlaid with the results from the α sweep at 10 deg, where servo position 215 is clearly optimal. Further cambering past this point to position 250 seems to induce flow separation and a minor loss in lift. The genetic algorithm quickly moves to the area of the design space between positions 200 and 250 (only indicated in Fig. 10 by the cluster of data points in this region), but ultimately settles on position 250 as optimal. We are thus left to conclude that the superiority of position 215 over 250 noted in the α-sweep tests has been affected by some form of hysteresis, though the difference in performance between the two is less than 2%. The majority of the final population resides at servo position 250, with the exception of two designs at position 180, presumably a result of the reproduction/mutation rates employed by the genetic algorithm. Two more genetic-algorithm runs at 10 deg produce very similar results, consistently converging to a position between 240 and 250.

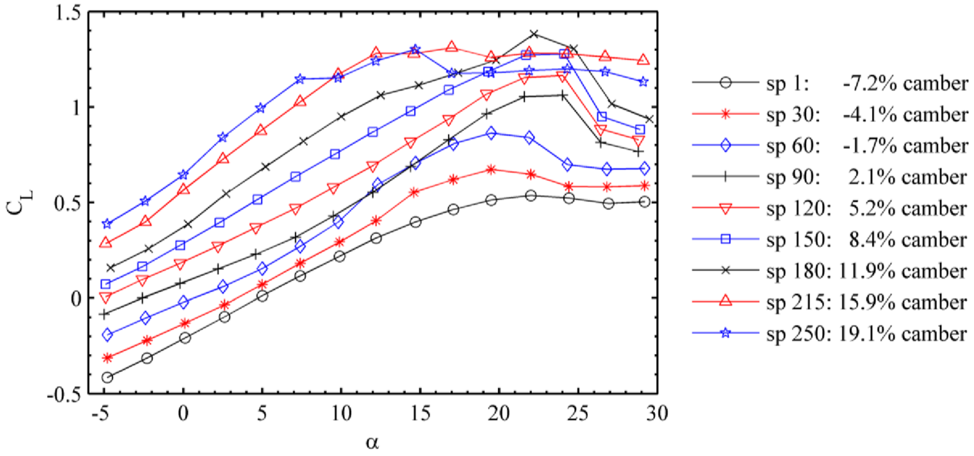

Fig. 7 Relationship of C_L–α as a function of servo actuation at $U_\infty = 16$ m/s.

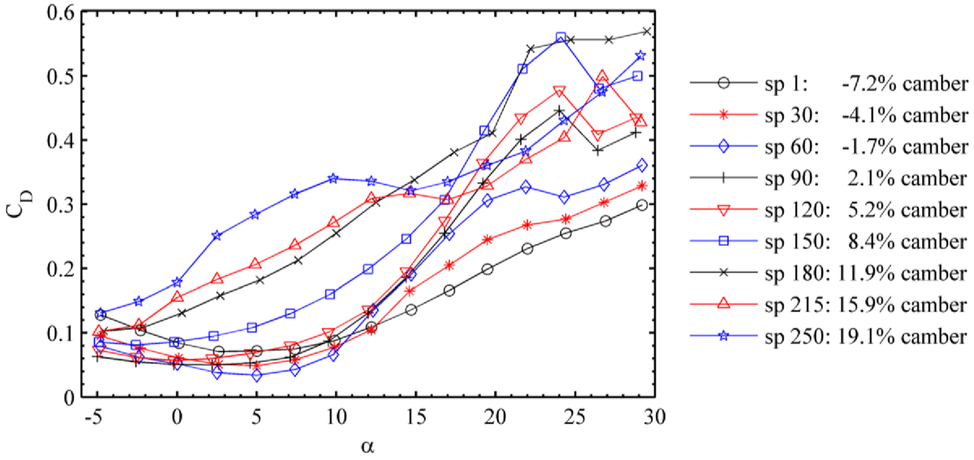

Fig. 8 Relationship of C_D–α as a function of servo actuation at $U_\infty = 16$ m/s.

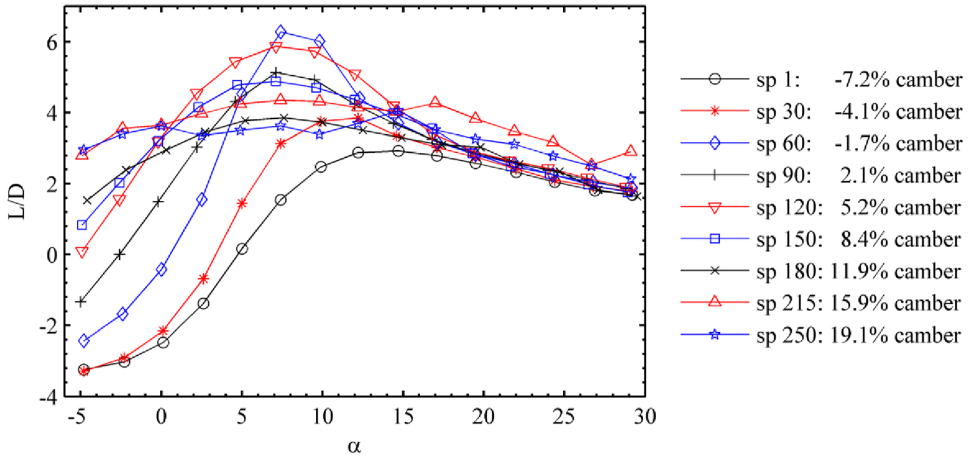

Fig. 9 Relationship of L/D–α as a function of servo actuation at $U_\infty = 16$ m/s.

Similar data are given in Fig. 11 for maximizing the aerodynamic efficiency at a 10 deg angle of attack. As before, a population size of 11 is used, and a suitable convergence is achieved after 13 generations. Whereas the correlation between the genetic-algorithm function evaluations and the α sweep is very good for the coefficient of lift, there is a considerable amount of scatter in both data sets' L/D, ostensibly due to the error contribution from both the lift and drag measurements. The genetic algorithm converges to an intermediate servo position 125 (again indicated by the large data cluster), though a significant volume of data points lie in the range between 125 and 150, as does the final population reported in Fig. 11.

As noted previously, the α-sweep tests indicate an optimal design at servo position 60, an apparent discontinuity in the L/D response surface. The cause of the discrepancy between the GA and α-sweep results is unclear: hysteresis may distort the data (as suspected in the preceding tests to locate the maximum C_L), or perhaps the response discontinuity at servo position 60 is narrow enough to remain undetected by the uniform initial distribution of designs. Regardless

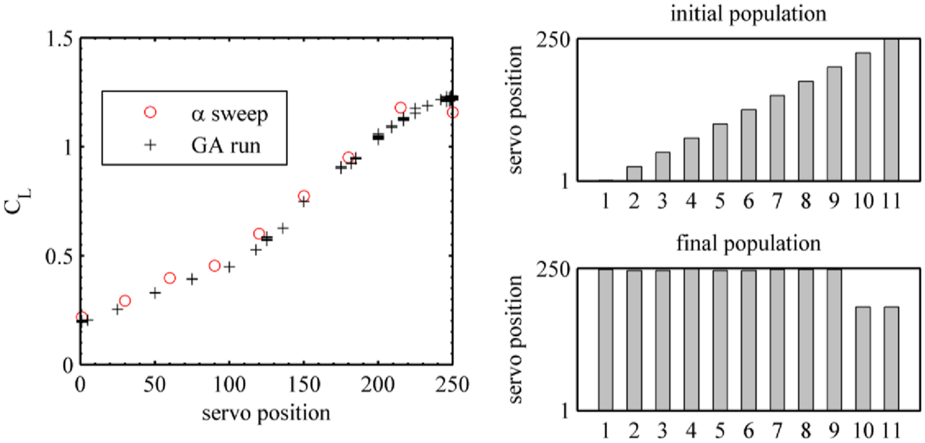

Fig. 10 Evolutionary optimization of C_L at $\alpha = 10$ deg and $U_\infty = 16$ m/s: function evaluations (left) and the initial/final design populations (right).

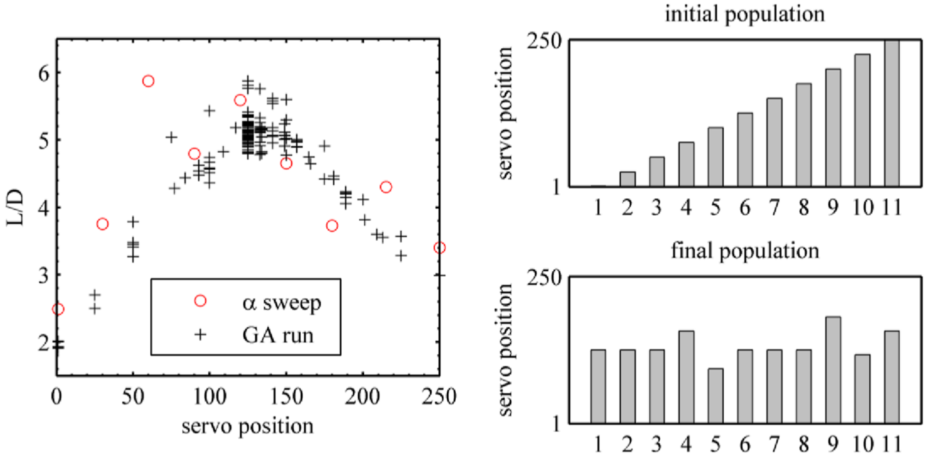

Fig. 11 Evolutionary optimization of L/D at $\alpha = 10$ deg and $U_\infty = 16$ m/s: function evaluations (left) and the initial/final design populations (right).

of the reason, the difference in the performance of the optimal design located by the genetic algorithm is again small: less than 5%. Two additional GA runs confirm a convergence at servo position 125. Additional tests to maximize L/D are also run at -5 and 0 deg. The former angle converges to servo position 230 (in good agreement with the data of Fig. 9), whereas the latter converges to position 160 (the measured L/D of 4.2 at this angle is a significant improvement over any of the designs tested within the α sweep).

IV. Multilevel Actuation Morphing Wing Optimization

A. Model Description

As the results in the previous section have demonstrated a certain degree of confidence in the hardware-in-the-loop optimization procedure, the technique is now used on a more realistic wing platform with multiple levels of actuation. A single layer of plain-weave carbon fiber is used to fabricate a Zimmerman planform wing (a common planform for micro air vehicle applications), with fibers running in the ±45 deg directions. Curved unidirectional strips of carbon fiber are again used to effectively transfer the wing shape from the root to the tip. The randomly speckled wing (for VIC purposes) can be seen in Fig. 12; the root chord is 17.5 cm, the wing span is 40.6 cm, the aspect ratio is 2.9, and the wing area is 567 cm^2. The estimated chord-based Reynolds number for this vehicle is 180,000, a slightly lower value than that seen in the previous section.

As before, two actuation points are used: one at the leading edge (permitting mostly rotation) and a second at the trailing edge, which allows for both rotation and longitudinal translation. The latter effect prevents the mechanism from becoming overconstrained, decreasing the resistance seen by each morphing servo. A flat mounting platform is again used to house the servos and actuation linkages and as a

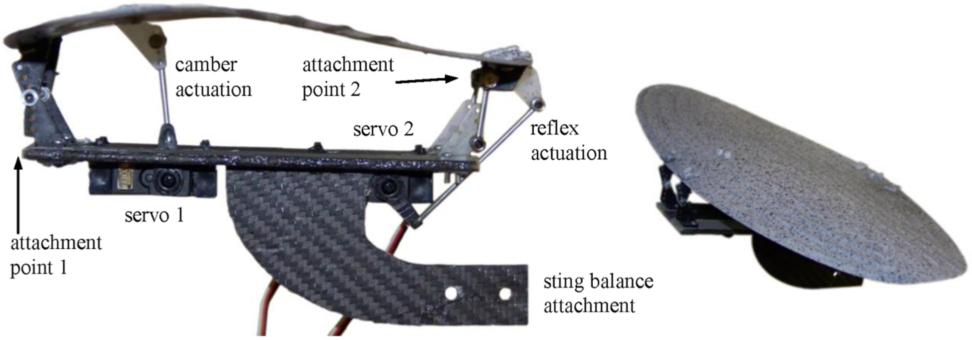

Fig. 12 Two-design-variable morphing Zimmerman wing.

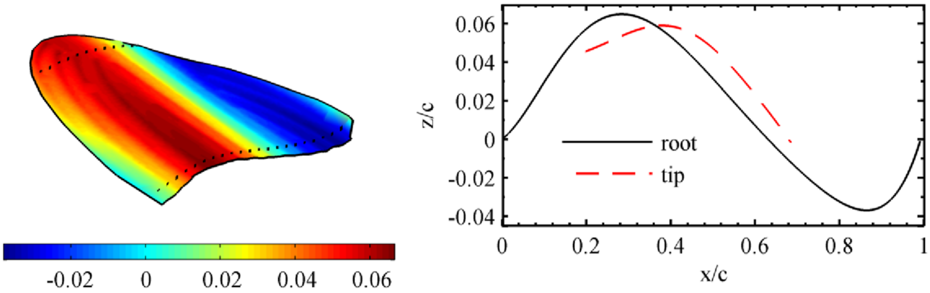

Fig. 13 Measured wind-off wing surface z/c at servo position (250, 250), with sections plotted at the root and the tip.

reference for angle-of-attack measurements. The first servo actuates the wing at $x/c = 0.21$; this is largely a vertical motion to provide wing camber. A second servo actuates the trailing edge, providing a rotation for potential wing reflex or negative camber. Introducing negative camber to a portion (typically toward the trailing edge) of the wing's root will surely decrease the overall lift, but such a shape has certain advantages, particularly for micro air vehicle wings. Decreasing the lift will likewise temper the induced drag of the wing, for which the relatively low aspect ratio (2.9) leaves a considerable portion of the longitudinal flow affected by the tip-vortex swirling structures. Reflex may also be used to reverse the sign of the adverse pressure gradient over the upper surface of the wing, prompting flow reattachment or perhaps completely preventing separation at a certain angle of attack. Though only lift and drag are under consideration for the current work, a reflex airfoil can provide longitudinal static stability without the use of a horizontal stabilizer (the negative lift over the reflex can offset the nose-down pitching moment of the remainder of the wing), for which the removal may be necessitated by micro air vehicle size constraints.

Full-field VIC results (z/c) of a cambered wing with trailing-edge reflex are given in Fig. 13, with airfoil sections plotted at the root and toward the wingtip. As expected, the curved carbon fiber stiffeners are less successful (than the rectangular wing) at transferring the same shape from root to wingtip. A slight loss in camber is observed, along with a shift toward the trailing edge. The choice of wing planform precludes the transferal of reflex to the wingtip, where the airfoil is only positively cambered. An array of the model's morphing potential can be seen in Fig. 14. Servo 1 is capable of ±11% camber, whereas servo 2 is capable of ±4% reflex. As before, large servo 1 positions increase the camber, though the opposite (inverse) of this shape can now be obtained from the servo's minimum position. Large servo 2 positions actuate a negative pitching moment to the trailing edge, increasing the reflex. A flat plate is obtained with both servos in their middle positions (125, 125). Finally, as both the leading and trailing edge of the carbon fiber wing are fixed (as well as the intermediate location attached to servo 1), wing aeroelasticity is not considered to be significant and will not be examined.

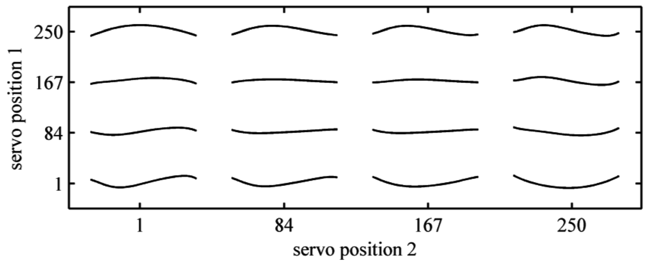

Fig. 14 Measured wind-off root airfoils of the two-design-variable morphing wing model.

B. Optimal-Lift Designs

The optimization procedure is carried out to maximize the lift of the morphing wing for a range of angles of attack from −5 to 20 deg in 5 deg increments. Testing above 20 deg invariably causes wing stall and excessive vibrations; function evaluation repeatability is very low and the genetic algorithm struggles to locate an optimum. To improve the convergence characteristics of the genetic algorithm operating with an increased number of design variables, the population size is increased to 25. The initial population is uniformly distributed over the design space, as before. Results at a 10 deg angle of attack are given in Fig. 15, in terms of the evolutionary history (both the mean lift across the population and the best are given at each generation) and the designs that populate the initial and final generations. For this case, convergence is very rapid, with little variation in the best design throughout the entire optimization. The majority of the population has converged upon this optimal design within 5 generations, and the function evaluations appear to be very clean and repeatable (as previously noted in Fig. 10). The optimal design lies approximately at (170, 1), with a moderate amount of camber from servo 1 and no reflex from servo 2, which would only serve to decrease lift, as discussed previously. Careful evaluation of the initial population reveals that design number 9 is very close to this

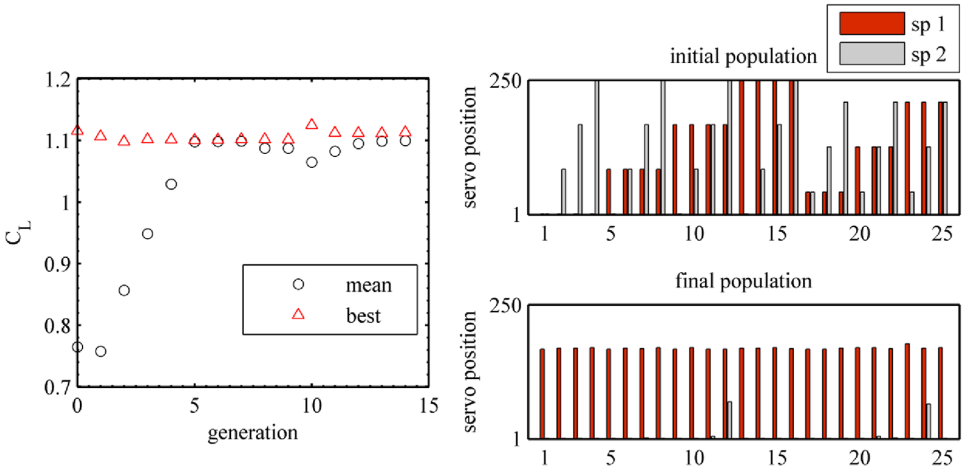

Fig. 15 Evolutionary optimization of C_L at $\alpha = 10$ deg and $U_\infty = 16$ m/s: convergence history (left) and the initial/final design populations (right).

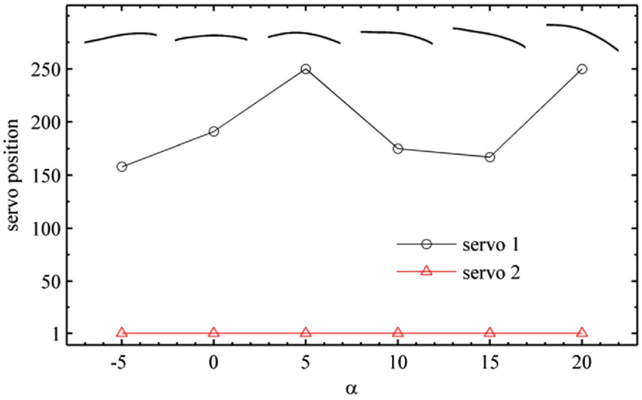

Fig. 16 Morphing wing shapes and servo positions for maximum lift through an α sweep at $U_\infty = 16$ m/s.

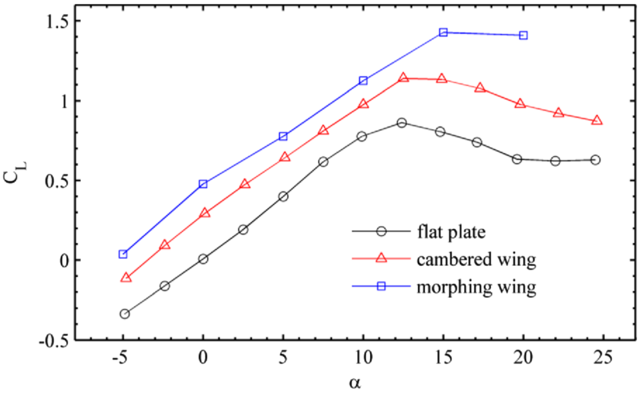

Fig. 17 Morphing wing lift performance versus a flat plate and a cambered airfoil.

optimum. The elitism employed within the genetic algorithm ensures that this design is preserved from one generation to the next.

The morphing wing shapes found to optimize lift at all six of the tested angles of attack are given in Fig. 16. The measured performance is given in Fig. 17, for comparison with the wing morphed into a flat plate (125, 125) and an intermediate wing at servo positions (250, 110). The moderate trailing-edge actuation of the latter airfoil pushes the maximum camber to $x/c = 0.4$, a shape commonly seen on micro air vehicles, and thus a good model for comparison purposes. As expected, none of the optimal-lift designs use any reflex actuation from servo 2; the position is fixed at the minimum (1) throughout the α sweep. For low angles of attack, camber from servo 1 is progressively increased to optimize lift, in accordance with linear theory. Flow separation clearly becomes an issue above 10 deg, as the optimizer is forced to employ a moderate camber; this effect can also be seen in Fig. 7 with the one-design-variable morphing wing. The optimal designs are identical at 5 and 20 deg, both calling for the largest camber. The adaptive morphing wing consistently outperforms both the flat plate and the cambered wing. Despite the aerodynamic twist of the morphing wing, all three wings have approximately the same prestall lift slope. Maximizing the lift has the unexpected consequence of improving the stalling behavior as well. In spite of a larger maximum possible lift coefficient, stall is delayed by roughly 3 deg, as compared with the other two cases, and characterized by a very benign stall, with little loss of lift between the 15 and 20 deg angles of attack.

C. Optimal Efficiency Designs

Similar tests are run to maximize the wing efficiency, again using a population size of 25 with the initial population uniformly distributed within the design space. The genetic algorithm is run between −5 and 5 deg angles of attack in 2.5 deg increments and at 10 and 15 deg as well. The evolutionary history, initial population, and final population found at 10 deg are given in Fig. 18. As expected from the measurement repeatability issues discussed for the preceding single-design-variable model, convergence of the lift-to-drag ratio is much noisier than that found for the lift. Unlike the previous case, a member of the initial population does not lie very close to the optimum, and the best design of each generation changes several times throughout the optimum. Despite the variability in the best design's performance from one iteration to the next, its actual identity only changes 3 times: at iterations 7, 12, and 15. The flat plateaus of the best design's performance typically seen in GA runs with numerical objective functions (due to elitism) are destroyed here by experimental repeatability errors (though the pseudorandom variations in the mean performance is indicative of a healthy distribution throughout the design space). The genetic algorithm shows suitable convergence after 21 iterations, locating servo position (247, 156), a cambered wing with a very small amount of reflex toward the trailing edge. At this point, the best design in each generation has remained unchanged for 7 iterations, with almost no variability throughout the population for the last 3 iterations (as seen in the final population of Fig. 18). Further iterations would rely solely on the mutation operator for greater improvements in the aerodynamic efficiency.

The morphing wing shapes found to optimize L/D at all 7 of the tested angles of attack are given in Fig. 19, and the measured performance is given in Fig. 20 for comparison with the flat plate and cambered wing described previously. As before, the camber actuation provided by servo 1 does not drastically change throughout the α sweep, staying in a range between positions 150 and 250. Increasing the angle of attack from −5 to 2.5 deg increases the amount of reflex employed by the model to optimize L/D. Such a

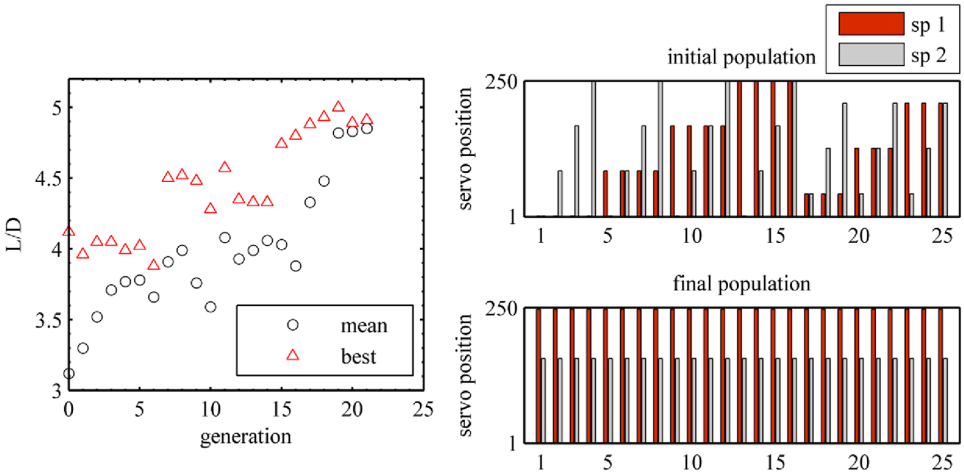

Fig. 18 Evolutionary optimization of L/D at $\alpha = 10$ deg and $U_\infty = 16$ m/s: convergence history (left) and the initial/final design populations (right).

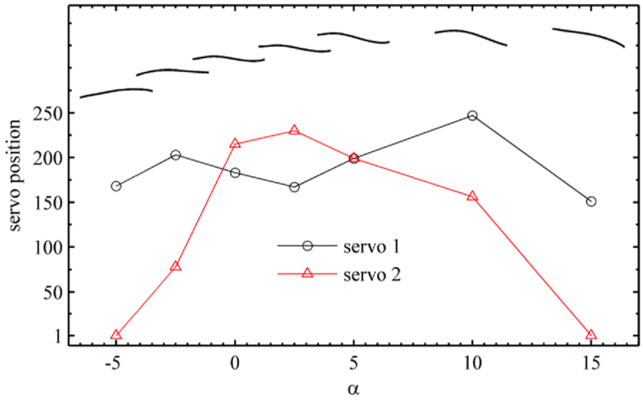

Fig. 19 Morphing wing shapes and servo positions for maximum L/D through an α sweep at $U_{\infty} = 16\ \mathrm{m/s}$.

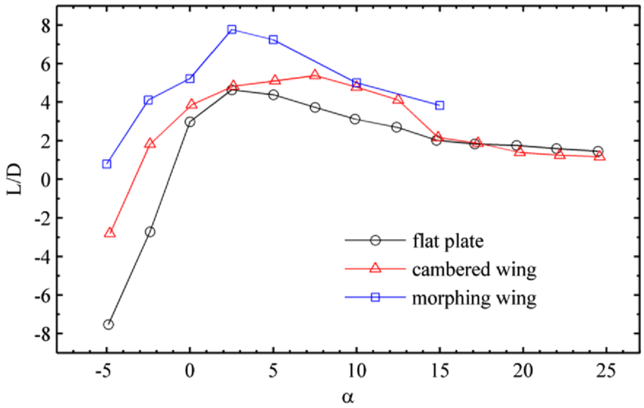

Fig. 20 Morphing wing L/D performance versus a flat plate and a cambered airfoil.

doubly cambered geometry obviously decreases the lift, but it is unclear whether the drag is tempered through viscous (flow reattachment forced by a favorable pressure gradient) or pressure (loss of lift leading to a subsequent drop in the tip-vortex strength) considerations. Between 0 and 5 deg angles of attack, the differences in the optimal shape are minor, though further increase in the incidence begins to remove the reflex from the wing. At 15 deg, the reflex is completely gone, with servo 2 now pushing the wing upward. This, coupled with a mild amount of camber from servo 1, provides a very counterintuitive wing shape, with a relatively flat leading edge and the wing camber shifted back to $x/c = 0.65$. A similar shape is used at a -5 deg angle of attack. One possible explanation for such a shape can be found in the design of low-speed laminar airfoils, in which the maximum thickness/camber is placed farther aft than usual to delay the location of the flow separation that is certain to occur against an adverse pressure gradient at low Reynolds numbers. Substantial improvements in the performance of the morphing wing can be seen in Fig. 20 for all of the angles of attack tested, with the exception of 10 deg (for which the cambered airfoil used for comparison is very similar in shape to the optimal design).

V. Conclusions

A procedure was established to achieve proper shape management of morphing wing structures using a genetic algorithm with wind-tunnel hardware in the loop to optimize the lift and the efficiency. A detailed examination of the entire design space of a morphing wing with a single actuation point was used to verify the optimization process. A morphing wing structure with two actuation points provided a more practical set of optimal designs that effectively use doubly cambered airfoils to control the lift-to-drag ratio. The largest barrier to the use of genetic algorithms with experimental objective functions is repeatability and error, thought to be primarily due to aerodynamic/electrical hysteresis encountered at the low testing Reynolds numbers. The elitism commonly employed in genetic algorithms will automatically copy the best designs from one generation to the next, but experimental error may prevent sequential measurements of the superior performance, delaying optimization convergence.

For the two examples considered here, the genetic-algorithm-based technique will not outperform (in terms of fewer function evaluations) conventional experimental optimization techniques such as design of experiments. Dividing each servo actuation sweep into 10 increments for a full factorial design of the morphing wing structure with two actuation points requires 100 function evaluations to fit a response surface and locate an optimum. For the wing efficiency optimization, the GA requires 21 generations to converge with a population size of 25 (525 function evaluations). This discrepancy becomes less true with the addition of further design variables, however; with five modes of wing actuation, for example, the hardware-in-the-loop optimization may be the only feasible method of properly exploring the experimental design space (the size of the factorial matrix will grow exponentially: 10^5 function evaluations for the example given). Micro and unmanned air vehicles are well suited for multiple levels of actuation: the flexible materials commonly used and the small flight loads allow for significant changes in shape with a relatively low amount of power. Effective shape management of a vehicle with multiple levels of actuation is outlined in the techniques described previously and may be the best method for maximizing the performance of a morphing wing.

Future work will include the use of laser-based flow visualization to document the flow patterns over the morphing wing during hysteresis testing and genetic-algorithm testing. Flow separation and reattachment are obvious points of interest, in the hope of elucidating the performance of the optimal wing designs. Further optimization runs will be conducted under various constraints: maximizing lift or efficiency with minimum bounds on the drag or the pitching moment (of particular interest to the static stability of the vehicle). Using these constraints at high angles of attack could result in the mitigation of wing stall or could yield a controlled-descent flight mode that is useful in autoland features. A genetic algorithm has no natural method for handling constraints, necessitating the use of penalty factors to the objective function for infeasible designs.

As discussed previously, morphing wings with large numbers of actuation points will be built and tested. The individual or simultaneous use of several distinct actuation modes is very realizable: the multipoint aerodynamic twist used here, but also variable aspect ratio (through a telescoping mechanism, perhaps), propeller thrust line, wing sweep (multiple joints can be considered for different inboard and outboard angles), and geometric wing twist. Finally, the optimization results will be used in an onboard control system for real-time wing morphing. Such a control system will receive instantaneous angle of attack and wind speed measurements and, in response, will command the series of actuators to optimize a given objective function (which may be determined based upon the current flight mode). This will be done using data similar to those seen in Figs. 16 and 19, either in terms of a lookup table or by fitting the optimal servo positions with a response surface. The former may require rounding the measured onboard angle of attack to the nearest optimization data point, whereas the latter requires interpolating between optimization data points.

Acknowledgments

This work is supported by U.S. Air Force contracts FA8651-04-C-0234 and F49620-03-1-0381.

References

[1] Videler, J., *Avian Flight*, Oxford Univ. Press, Oxford, 2005.

[2] Davidson, J., Chwalowski, P., and Lazos, B., "Flight Dynamics Simulation Assessment of a Morphable Hyper-Elliptic Cambered Span Winged Configuration," AIAA Paper 2003-5301, 2003, 2007.

[3] Abdulrahim, M., Garcia, H., and Lind, R., "Flight Characteristics of Shaping the Membrane Wing of a Micro Air Vehicle," *Journal of Aircraft*, Vol. 42, No. 1, 2005, pp. 131–137.
doi:10.2514/1.4782

[4] Bohn, C., "Dynamic Antifouling Structures and Actuators using EAP Composites," Ph.D. Dissertation, Dept. of Materials Science and Engineering, Univ. of Florida, Gainesville, FL, 2004.

[5] Bilgen, O., Kochersberger, K., Diggs, E., Kurdila, A., and Inman, D., "Morphing Wing Aerodynamic Control via Macro-Fiber-Composite Actuators in an Unmanned Aircraft," AIAA Paper 2007-2741, 2007.

[6] Strelec, J., Lagoudas, D., Khan, M., and Yen, J., "Design and Implementation of a Shape Memory Alloy Actuated Reconfigurable Airfoil," *Journal of Intelligent Material Systems and Structures*, Vol. 14, Nos. 4–5, 2003, pp. 257–273.
doi:10.1177/1045389X03034687

[7] Hicks, R., Murman, E., and Vanderplaats, G., "An Assessment of Airfoil Design by Numerical Optimization," NASA, TM X-3092, 1974.

[8] Lian, Y., Shyy, W., and Haftka, R., "Shape Optimization of a Membrane Wing for Micro Air Vehicles," *AIAA Journal*, Vol. 42, No. 2, 2004, pp. 424–426.
doi:10.2514/1.9106

[9] Obayashi, S., and Tsukahara, T., "Comparison of Optimization Algorithms for Aerodynamic Shape Design," *AIAA Journal*, Vol. 35, No. 8, 1997, pp. 1413–1415.
doi:10.2514/2.251

[10] Namgoong, H., Crossley, W., and Lyrintzis, A., "Aerodynamic Optimization of a Morphing Airfoil Using Energy as an Objective," *AIAA Journal*, Vol. 45, No. 9, 2007, pp. 2113–2124.
doi:10.2514/1.24355

[11] Drela, M., "XFOIL: An Analysis and Design System for Low Reynolds Number Airfoils," *Low-Reynolds Number Aerodynamics*, Springer–Verlag, New York, 1989, pp. 1–12.

[12] Naujoks, B., Willmes, L., Back, T., and Haase, W., "Evaluating Multi-Criteria Evolutionary Algorithms for Airfoil Optimization," *Lecture Notes in Computer Science*, Vol. 2439-2000, 2000, pp. 841–850.

[13] Haney, H., and Johnson, R., "Application of Numerical Optimization to the Design of Wings with Specified Pressure Distributions," NASA, CR 3238, 1980.

[14] Gopalarathnam, A., and Selig, M., "Low-Speed Natural-Laminar-Flow Airfoils: Case Study in Inverse Airfoil Design," *Journal of Aircraft*, Vol. 38, No. 1, 2001, pp. 57–63.
doi:10.2514/2.2734

[15] Peng, F., Hu, Y., and Ng, A., "Experimental Study of Active Shape Control of Membrane Structures Using Genetic Algorithms," *International Astronautical Congress*, Vancouver, Canada, International Astronautical Federation Paper IAC-04-1[1].4.07, Oct. 2004.

[16] Hemker, T., Sakamoto, H., Stelzer, M., and von Stryk, O., "Hardware-in-the-Loop Optimization of the Walking Speed of a Humanoid Robot," *International Conference on Climbing and Walking Robots*, CLAWAR Association, Sheffield, England, U.K., 12–14 Sept. 2006.

[17] Hunt, R., Hornby, G., and Lohn, J., "Toward Evolved Flight," *Genetic and Evolutionary Computation Conference*, Association for Computing Machinery, New York, 25–29 June 2005, pp. 957–964.

[18] Levinsky, E., and Palko, R., "Tests of an Improved Computer-Controlled, Self-Optimizing Variable-Geometry Wing," AIAA Paper 1982-599, 1982.

[19] Haftka, R., and Gurdal, Z., *Elements of Structural Optimization*, Kluwer Academic, Dordrecht, The Netherlands, 1992.

[20] Chipperfield, A., Fleming, P., Polheim, H., and Fonseca, C., "A Genetic Algorithm Toolbox for MATLAB," *International Conference on Systems Engineering*, Coventry, England, U.K., May 16–21, 1994.

[21] Sutton, M., Cheng, M., Peters, W., Chao, Y., and McNeill, S., "Application of an Optimized Digital Image Correlation Method to Planar Analysis," *Image and Vision Computing*, Vol. 4, No. 3, 1986, pp. 143–151.
doi:10.1016/0262-8856(86)90057-0

[22] *Recommended Practice: Calibration and Use of Internal Strain-Gauge Balances with Application to Wind Tunnel Testing*, R-091-2003, AIAA Standards Series, AIAA, Reston, VA, 2003.

[23] Mueller, T., "The Influence of Laminar Separation and Transition on Low Reynolds Number Airfoil Hysteresis," *Journal of Aircraft*, Vol. 22, No. 9, 1985, pp. 763–770.
doi:10.2514/3.45199

J. Samareh
Associate Editor